Journal of Science and Transport Technology
Journal homepage: https://jstt.vn/index.php/en

# Nonlinear Stability of FG-GPLRC Shallow Annular Spherical Caps and Annular Plates Stiffened by Circumferential Stiffener System

Nguyen Thi Thanh Hoai[1,2], Dang Thuy Dong[3,4], Cao Van Doan[5,*]
[1]Faculty of International Education, University of Transport and Communications, Hanoi, Vietnam
[2]Graduate University of Science and Technology, Vietnam Academy of Science and Technology, Hanoi, Vietnam
[3]Mechanics of Advanced Materials and Structures, Institute for Advanced Study in Technology, Ton Duc Thang University, Ho Chi Minh City, Vietnam
[4]Faculty of Civil Engineering, Ton Duc Thang University, Ho Chi Minh City, Vietnam
[5]Mechanics of Advanced Materials and Structures, University of Transport Technology, Hanoi, Vietnam

**Article info**
**Type of article:**
Original research paper

**DOI:**
https://doi.org/10.58845/jstt.utt.2025.en.5.4.126-140

***Corresponding author:**
Email address:
doancv@utt.edu.vn

**Received:** 12/09/2025
**Received in Revised Form:** 10/11/2025
**Accepted:** 12/12/2025

**Abstract:** For the first time, an analytical approach to the static stability problem of a shallow annular spherical cap stiffened by a system of circumferential stiffeners is presented in this study. Both the shell and the stiffeners are constructed from Functionally Graded Graphene Platelet Reinforced Composite (FG-GPLRC) material, which follows five common distribution laws: FG-X, FG-O, FG-A, FG-V, and UD. The stiffened shallow annular spherical caps are subjected to a uniform temperature change. An extended smeared stiffener technique is applied to the circumferential stiffener system of the SASC. Based on Donnell's classical shell theory and von Kármán geometric nonlinearities, the fundamental expressions and governing equations of the problem are established. Novel displacement solutions satisfying the parallel-closed conditions are proposed. The load–deflection relationships are derived by applying the Ritz energy minimization method. Consequently, the significant effects of the stiffeners, material model, and geometric and material parameters are investigated.

**Keywords:** Nonlinear stability, Shallow Annular Spherical Caps, Circumferential Stiffener System, Asymmetrical deformation, Ritz energy method.

## 1. Introduction

Shallow spherical caps (SSCs), circular plates (CPLs), shallow annular spherical caps (SASCs), and annular plates (APLs) are commonly used structures in many engineering fields. They are often found in various civil structures, mechanical equipment, and parts of aerospace equipment.

The analysis of the mechanical behavior of isotropic SSCs and CPLs has been carried out by many researchers, making it a noteworthy research direction. Kalnins and Naghdi [1], Grossman et al. [2], and Sathyamoorthy [3] focused on the vibration analysis of isotropic SSCs

based on various models and theories. Dube et al. [4] employed the first-order shear deformation theory (FSDT) and the Galerkin method to analyze the nonlinear static and dynamic behavior of thick SSCs. The buckling behavior of pressurized SSCs was numerically investigated by Wang et al. [5]. Du et al. [6] introduced a unified formulation for free vibration analysis of edge-restrained SSCs with both uniform and stepped thicknesses. Li et al. [7] investigated the nonlinear axisymmetric bending model of a strain gradient thin circular plate. Ismail et al. [8] studied the most critical buckling scenarios in SSCs using numerical simulations.

For FGM CPLs, several authors [9–12] have studied the static and dynamic buckling and vibration responses under various loading conditions using different methods. For FGM SSCs, Ahmadi and Foroutan [13] investigated the nonlinear dynamic buckling responses of porous FGM SSCs. Based on the Timoshenko-Mindlin hypothesis, Fu et al. [14] investigated the transient deformation of FGM SSCs subjected to time-dependent thermomechanical load. Applying the Galerkin method and FSDT, Bich and Tung [15] studied the nonlinear axisymmetric buckling of FGM SCs, Anh and Duc [16] analyzed the nonlinear thermo-mechanical stability of thick S-FGM SSCs, and Phuong et al. [17] analyzed the sandwich FGM SSCs in a nonlinear forced vibration problem. Ly et al. [18] analyze thermo-mechanical buckling in FGM CPLs and SSCs with porous core based on higher-order shear deformation theory (HSDT) and the energy method. Barzegar and Fadaee [19] explored the free vibration and buckling responses of thin FGM shallow SSCs under a thermal load based on a decoupling technique.

For FG-GPLRC CPLs and SSCs, Javani et al. [20] and Chu et al. [21] investigated vibration and stability responses of the FG-GPLRC CPLs using FSDT and HSDT, respectively. Chien and Phuc [22] studied the free vibration behavior of FG-GPLRC CPLs using the HSDT and meshfree method. The dynamic instability responses of FG-GPLRC CPLs were mentioned by Dai et al. [23]. Heydarpour et al. [24] presented thermoelastic behavior of FG-GPLRC SSCs using the Lord-Shulman theory. Liu et al. [25] studied the linear and nonlinear free vibration problems of FG-GPLRC SSCs and CPLs using the 3D elasticity theory. Using the energy method, the nonlinear static and dynamic responses of FG-GPLRC/ sandwich FG-GPLRC CPLs and SSCs were investigated by Phuong et al. [26], Tu et al. [27], and Ly et al. [28], respectively. The FG-GPLRC CPLs and SSCs stiffened by spiderweb stiffeners were considered in the nonlinear thermo-mechanical buckling [29], static and dynamic buckling [30], and vibration [31] problems.

Although not as commonly studied as shallow spherical shells and circular plates, the stability and dynamics of SASCs and APLs have also been investigated by several authors. APLs were also considered in the symmetric and asymmetric vibration problems [32-34], with laminated composites [32], with thermal rotating conditions [33], and with general boundary conditions [34]. The segments of FGM SASCs stiffened by parallel stiffeners were investigated in linear buckling by Nam et al. [35], using the Galerkin method and adjacent equilibrium criterion. Mirjavadi et al. [36] studied the nonlinear vibration of segments of FGM SASCs using the Galerkin method and Donnell shell theory. Vibration and dynamic behaviors of FG-GPLRC APLs were presented using the Rayleigh-Ritz variational method [37] and the generalized differential quadrature method [38, 39]. Safarpour et al. [40] studied three-dimensional bending and frequency of FG-GPLRC porous CPLs and APLs on different boundary conditions.

It can be seen that there are extensive studies on the mechanical response of CPLs and SSCs, but studies on APLs and SASCs are still very limited. Especially, FG-GPLRC APLs and SASCs reinforced with circumferential FG-GPLRC stiffeners have not been studied yet. In this study, the nonlinear thermal buckling and postbuckling

responses of FG-GPLRC APLs and SASCs stiffened by circumferential stiffeners are investigated in detail. An improved smeared stiffener technique is developed for the FG-GPLRC circumferential stiffener system to obtain asymmetric responses. Trigonometric solutions of displacement components satisfying the parallel closed condition are proposed. The governing equations of stiffened SASCs/APLs are solved by applying the energy method. The effects of stiffeners, material distribution models, and geometric and material parameters are investigated in the numerical examples.

## 2. Modeling of FG-GPLRC SASCs stiffened by circumferential stiffener system

An asymmetrically deformed SASCs is considered in this paper. The SASC is subjected to temperature changes, as described in Fig. 1, with the thickness of the SASC $h$, curvature $R$, and the radii of the upper and lower bases are denoted by $r_t$ and $r_b$, respectively. A circumferential stiffener system is applied to the asymmetrical SASC. It can be seen in Fig. 1, the shell is analyzed using a coordinate system $(\varphi, \theta, z)$, where $\varphi$ aligns with the meridian, $\theta$ with the parallel direction, and $z$ with the thickness direction.

The SASCs and their corresponding stiffeners are both constructed from FG-GPLRC. To ensure continuity of material in the shell and stiffener, five material models are considered as follows (Fig. 2 and Table 1).

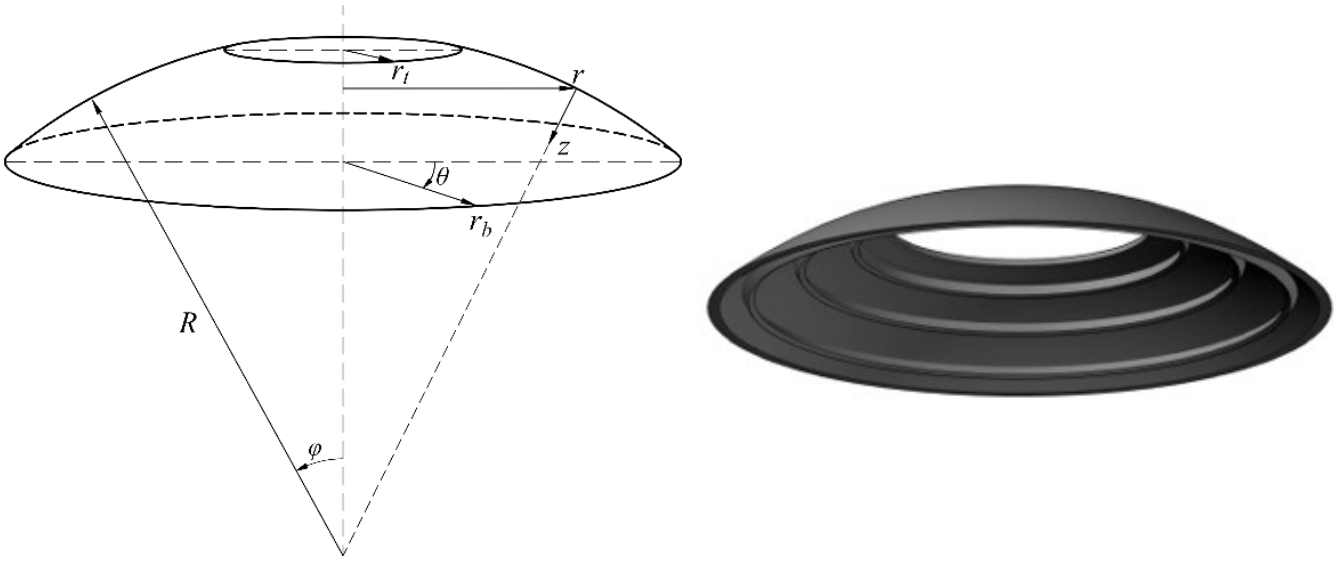


**Fig 1.** Model and coordinate system of stiffened FG-GPLRC SASC

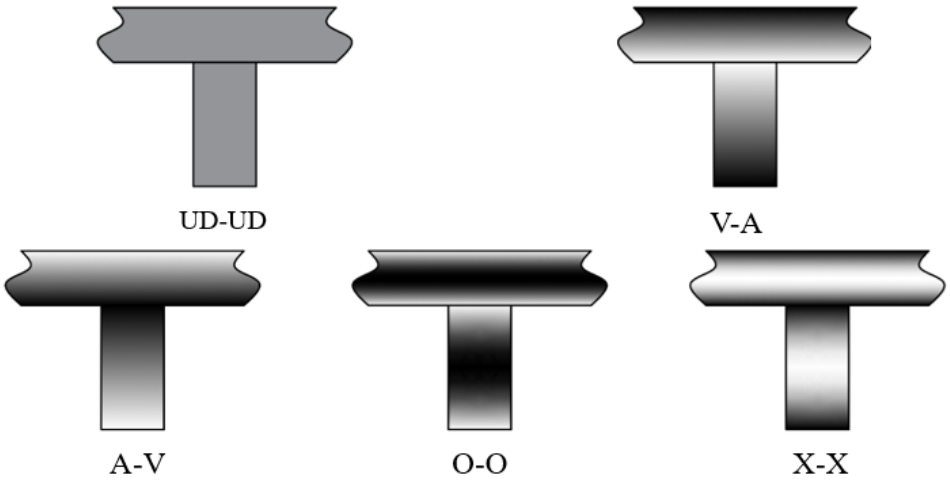


**Fig 2.** Material models of shell and stiffeners of SASC/APL

**Table 1**. Model of SASC and Stiffener material

| Model | SASC material | Stiffener material |
|---|---|---|
| V-A | FG-V type | FG-A type |
| X-X | FG-X type | FG-X type |
| UD-UD | UD-UD type | UD-UD type |
| O-O | FG-O type | FG-O type |
| A-V | FG-A type | FG-V type |

For SASCs, the distribution of the GPL volume fraction through the shell thickness follows the rules described below (for $-h/2 \le z \le h/2$)

$$\omega_{GPL}^{sasc} = \begin{cases} \dfrac{-2z+h}{h}\omega_{GPL} & \text{FG-V type,} \\ \dfrac{4|z|}{h}\omega_{GPL} & \text{FG-X type,} \\ \omega_{GPL} & \text{UD type,} \\ \left(2-\dfrac{4|z|}{h}\right)\omega_{GPL} & \text{FG-O type,} \\ \dfrac{2z+h}{h}\omega_{GPL} & \text{FG-A type,} \end{cases} \quad (1)$$

For stiffeners, to preserve the continuity of materials within the stiffeners, the corresponding GPL volume fraction is defined by the expression below, (for $h/2 \le z \le h/2+h_{st}$).

$$\omega_{GPL}^{st} = \begin{cases} \left(\dfrac{2z-h}{h_{st}}\right)\omega_{GPL} & \text{FG-A type,} \\ \left|\dfrac{-4z+2h+2h_{st}}{h_{st}}\right|\omega_{GPL} & \text{FG-X type,} \\ \omega_{GPL} & \text{UD type,} \\ \left(2-\left|\dfrac{-4z+2h+2h_{st}}{h_{st}}\right|\right)\omega_{GPL} & \text{FG-O type,} \\ \left(\dfrac{-2z+h+2h_{st}}{h_{st}}\right)\omega_{GPL} & \text{FG-V type,} \end{cases} \quad (2)$$

where $\omega_{GPL}$ denotes the total mass fraction of GPLs distributed within both the SASC and the stiffeners.

The Halpin–Tsai scheme is employed to determine the elastic moduli of the cap skin and the stiffeners as [39]

$$E_{sasc} = \frac{E_m}{8}\left(\frac{3+3a_G a_E V_{GPL}^{sasc}}{1-a_E V_{GPL}^{sasc}} + \frac{5+5b_G b_E V_{GPL}^{sasc}}{1-b_E V_{GPL}^{sasc}}\right), \quad (3)$$

$$E_{st} = \frac{E_m}{8}\left(\frac{3+3a_G a_E V_{GPL}^{st}}{1-a_E V_{GPL}^{st}} + \frac{5+5b_G b_E V_{GPL}^{st}}{1-b_E V_{GPL}^{st}}\right), \quad (4)$$

where

$$V_{GPL}^{sasc} = \frac{\rho_m \omega_{GPL}^{sasc}}{\rho_m \omega_{GPL}^{sasc} + \rho_{GPL}\left(1-\omega_{GPL}^{sasc}\right)}, \quad (5)$$

$$V_{GPL}^{st} = \frac{\rho_m \omega_{GPL}^{sasc}}{\rho_m \omega_{GPL}^{st} + \rho_{GPL}\left(1-\omega_{GPL}^{st}\right)}, \quad (6)$$

and

$$a_E = \frac{E_{GPL}-E_m}{E_{GPL}+\delta_G E_m}, b_E = \frac{E_{GPL}-E_m}{E_{GPL}+b_G E_m}, \quad a_G = \frac{2l_G}{t_G}, b_G = \frac{2w_G}{t_G}, \quad (7)$$

with $V_{GPL}^{sasc}$ corresponds to the GPL volume fraction in the cap skin, while $V_{GPL}^{st}$ refers to that in the stiffeners. The properties of the matrix are given by $E_m$ (Young's modulus) and $\rho_m$ (density). Correspondingly, $E_{GPL}$ and $\rho_{GPL}$ are utilized for the GPLs. The shape of the GPLs is fully described by their dimensions: $w_G$ (width), $l_G$ (length) and $t_G$ (thickness).

The corresponding Poisson's ratios and thermal expansion coefficients for the cap skin and the stiffeners are given as

$$\nu_{sasc} = \nu_m\left(1-V_{GPL}^{sasc}\right) + \nu_{GPL}V_{GPL}^{sasc}, \quad \alpha_{sasc} = \alpha_m\left(1-V_{GPL}^{sasc}\right) + \alpha_{GPL}V_{GPL}^{sasc}, \quad (8)$$

$$\nu_{st} = \nu_m\left(1-V_{GPL}^{st}\right) + \nu_{GPL}V_{GPL}^{st}, \quad \alpha_{st} = \alpha_m\left(1-V_{GPL}^{st}\right) + \alpha_{GPL}V_{GPL}^{st}, \quad (9)$$

## 3. Fundamental equations

To facilitate the calculation process for SASCSs, the variable $r = R\sin\varphi$ representing the

parallel circle with the base, is utilized. Given that the SASCSs are shallow, the derivation of the fundamental formulas and governing equations in this research is based on two key elements: the application of a quasi-polar coordinate system and the geometric approximations $\cos\varphi \approx 1$ and $R d\varphi = dr$. The general expressions and governing equations provided below apply to SASCs, while those for APLs can be obtained by setting $R \to \infty$.

The mid-surface strain field of the SASCs can be determined by [35]

$$\begin{Bmatrix} \varepsilon_r^0 \\ \varepsilon_\theta^0 \\ \gamma_{r\theta}^0 \end{Bmatrix} = \begin{Bmatrix} u_{0,r} - \dfrac{w_0}{R} + \dfrac{1}{2} w_{0,r}^2 + w_{0,r} w_{1,r} \\ \dfrac{1}{r}(v_{0,\theta} + u_0) - \dfrac{w_0}{R} + \dfrac{1}{2r^2} w_{0,\theta}^2 + \dfrac{w_{0,\theta} w_{1,\theta}}{r^2} \\ r\left(\dfrac{v_0}{r}\right)_{,r} + \dfrac{u_{0,\theta}}{r} + \dfrac{w_{0,r} w_{0,\theta}}{r} + \dfrac{w_{0,r} w_{1,\theta}}{r} + \dfrac{w_{0,\theta} w_{1,r}}{r} \end{Bmatrix}. \quad (10)$$

where the variables $u_0$, $v_0$, and $w_0$ represent the displacement components at the middle surface. These displacements occur in the meridian, parallel, and thickness directions, respectively. In addition, $w_1(r)$ is used to denote the initial imperfection in deflection.

The strain field, at an arbitrary distance $z$ from the mid-surface, is defined as [35]

$$\begin{Bmatrix} \varepsilon_r \\ \varepsilon_\theta \\ \gamma_{r\theta} \end{Bmatrix} = -z \begin{Bmatrix} \kappa_r \\ \kappa_\theta \\ \kappa_{r\theta} \end{Bmatrix} + \begin{Bmatrix} \varepsilon_r^0 \\ \varepsilon_\theta^0 \\ \gamma_{r\theta}^0 \end{Bmatrix}, \quad (11)$$

where

$$\begin{Bmatrix} \kappa_r \\ \kappa_\theta \\ \kappa_{r\theta} \end{Bmatrix} = \begin{Bmatrix} w_{0,rr} \\ \dfrac{w_{0,r}}{r} + \dfrac{w_{0,\theta\theta}}{r^2} \\ \dfrac{w_{0,r\theta}}{r} - \dfrac{w_{0,\theta}}{r^2} \end{Bmatrix}, \quad (12)$$

Considering the influence of temperature variation, the constitutive stress–strain relationship for the SASCs is formulated as follows

$$\begin{bmatrix} \sigma_r \\ \sigma_\theta \\ \tau_{r\theta} \end{bmatrix} = \begin{bmatrix} C_{11} & C_{12} & 0 \\ C_{12} & C_{22} & 0 \\ 0 & 0 & C_{66} \end{bmatrix} \left( \begin{bmatrix} \varepsilon_r \\ \varepsilon_\theta \\ \gamma_{r\theta} \end{bmatrix} - \begin{bmatrix} \alpha \\ \alpha \\ 0 \end{bmatrix} \Delta T \right), \quad (13)$$

with $\Delta T$ denotes the difference in temperature from the undeformed state to the final thermally strained state, a value which is assumed as constant. $C_{ij}$ $(ij = 11,12,22,66)$ represents the reduced stiffnesses of stiffened SASCs.

In this work, the force and moment resultants of stiffened SASCs are obtained by extending Lekhnitskii's smeared stiffener method, formulated based on classical beam theory, wherein the stiffness of the shell skin is combined with that of the stiffeners. The resulting expressions are

$$\begin{Bmatrix} N_r \\ N_\theta \\ N_{r\theta} \\ M_r \\ M_\theta \\ M_{r\theta} \end{Bmatrix} = \begin{bmatrix} \bar{A}_{11} & \bar{A}_{12} & 0 & \bar{B}_{11} & \bar{B}_{12} & 0 \\ \bar{A}_{12} & \bar{A}_{22} & 0 & \bar{B}_{12} & \bar{B}_{22} & 0 \\ 0 & 0 & \bar{A}_{66} & 0 & 0 & \bar{B}_{66} \\ \bar{B}_{11} & \bar{B}_{12} & 0 & \bar{D}_{11} & \bar{D}_{12} & 0 \\ \bar{B}_{12} & \bar{B}_{22} & 0 & \bar{D}_{12} & \bar{D}_{22} & 0 \\ 0 & 0 & \bar{B}_{66} & 0 & 0 & \bar{D}_{66} \end{bmatrix} \begin{Bmatrix} \varepsilon_r^0 \\ \varepsilon_\theta^0 \\ \gamma_{r\theta}^0 \\ -\kappa_r \\ -\kappa_\theta \\ -\kappa_{r\theta} \end{Bmatrix} - \left( \begin{Bmatrix} \Phi_{1r} \\ \Phi_{1\theta} \\ 0 \\ \Phi_{2r} \\ \Phi_{2\theta} \\ 0 \end{Bmatrix} \Delta T \right) \quad (14)$$

where

$$\begin{aligned} &\left(\bar{A}_{11}, \bar{B}_{11}, \bar{D}_{11}\right) = \left(A_{11}^{sasc} + A_{11}^{st}, B_{11}^{sasc} + B_{11}^{st}, D_{11}^{sasc} + D_{11}^{st}\right), \\ &\left(\bar{A}_{22}, \bar{B}_{22}, \bar{D}_{22}\right) = \left(A_{22}^{sasc} + A_{22}^{st}, B_{22}^{sasc} + B_{22}^{st}, D_{22}^{sasc} + D_{22}^{st}\right), \\ &\left(\bar{A}_{12}, \bar{B}_{12}, \bar{D}_{12}\right) = \left(A_{12}^{sasc}, B_{12}^{sasc}, D_{12}^{sasc}\right), \\ &\left(\bar{A}_{66}, \bar{B}_{66}, \bar{D}_{66}\right) = \left(A_{66}^{sasc}, B_{66}^{sasc}, D_{66}^{sasc}\right), \end{aligned} \quad (15)$$

and

$$\begin{aligned} &\left(\Phi_{1r}, \Phi_{1\theta}\right) = \left(\Phi_{1r}^{sasc} + \Phi_{1r}^{st}, \Phi_{1\theta}^{sasc} + \Phi_{1\theta}^{st}\right), \\ &\left(\Phi_{2r}, \Phi_{2\theta}\right) = \left(\Phi_{2r}^{sasc} + \Phi_{2r}^{st}, \Phi_{2\theta}^{sasc} + \Phi_{2\theta}^{st}\right), \end{aligned} \quad (16)$$

with

$$\left(A_{ij}^{sasc}, B_{ij}^{sasc}, D_{ij}^{sasc}\right) = \int_{-h/2}^{h/2} \left(1, z, z^2\right) C_{ij}^{sasc} dz,$$

$$\left(A_{kl}^{st},B_{kl}^{st},D_{kl}^{st}\right)=\int_{h/2}^{h/2+h_{st}}\frac{b_{st}}{d_{st}}\left(1,z,z^2\right)C_{kl}^{st}dz, \quad (17)$$

$ij=11,12,22,66;\quad kl=11,22$

and

$$\left(\Phi_{1r}^{sasc},\Phi_{2r}^{sasc}\right)=\int_{-h/2}^{h/2}\left[\left(C_{11}^{sasc}+C_{12}^{sasc}\right)\alpha_{sasc}\right](1,z)dz,$$
$$\left(\Phi_{1\theta}^{sasc},\Phi_{2\theta}^{sasc}\right)=\int_{-h/2}^{h/2}\left[\left(C_{22}^{sasc}+C_{12}^{sasc}\right)\alpha_{sasc}\right](1,z)dz, \quad (18)$$

$$\left(\Phi_{1\theta}^{st},\Phi_{2\theta}^{st}\right)=\int_{h/2}^{h/2+h_{st}}\frac{b_{st}}{d_{st}}\left(C_{22}^{st}\alpha_{st}\right)(1,z)dz, \quad (19)$$

where

$$C_{11}^{sasc}=C_{22}^{sasc}=\frac{E_{sasc}}{1-\nu_{sasc}^2},\ C_{12}^{sasc}=\frac{E_{sasc}\nu_{sasc}}{1-\nu_{sasc}^2},$$
$$C_{66}^{sasc}=\frac{E_{sasc}}{2\left(1+\nu_{sasc}\right)},C_{11}^{st}=C_{22}^{st}=E_{st}, \quad (20)$$

where $b_{st}$ and $d_{st}$ represent the widths and the distances between two adjacent circumferential stiffeners, respectively. The superscripts sasc, st represent the shell and the stiffeners, respectively. with the symbols $b_{st}$ and $d_{st}$ denote the widths of the stiffeners and the distances between two neighboring stiffeners, respectively. For clarity, the superscripts sasc, and st are employed as notational identifiers for the cap and the stiffeners, respectively.

The total potential energy for the SASCs is expressed as

$$U_T=\frac{1}{2}\int_{\Omega}\int_{0}^{2\pi}\int_{r_t}^{r_b}\left\{\begin{matrix}\sigma_r\left[\varepsilon_r-\alpha(z)\Delta T\right]\\+\sigma_\theta\left[\varepsilon_\theta-\alpha(z)\Delta T\right]\\+\tau_{r\theta}\gamma_{r\theta}\end{matrix}\right\}rdrd\theta dz, \quad (21)$$

## 2. Boundary conditions and solution method

In this paper, the pinned boundary constraints applied to both the upper and lower parallel bases, the boundary conditions can be written as

$$w_0=0,\ u_0=0,\ M_r=0,\qquad \text{at } r=r_t,\ r_b, \quad (22)$$

The following approximate displacement formulations are proposed to satisfy both the parallel closed requirement in the parallel direction and the boundary condition (22), given by

$$u_0=U\sin(n\theta)\sin\left(\frac{2m\pi(r-r_t)}{r_b-r_t}\right),$$
$$v_0=V\sin(2n\theta)\sin\left(\frac{m\pi(r-r_t)}{r_b-r_t}\right), \quad (23)$$
$$w_0=W\sin(n\theta)\sin\left(\frac{m\pi(r-r_t)}{r_b-r_t}\right).$$

Here, the amplitudes of the meridional and parallel displacement components are denoted by $U$ and $V$, respectively, while the amplitude of the deflection is denoted by $W$. $m$ and $n$ denote the number of half-wave in the meridian direction and the number of full-wave in the parallel direction, respectively.

Assuming that the expression for the initial imperfection is taken similarly to the form of deflection, as follows

$$w_1=W^*\sin\left(\frac{m\pi(r-r_t)}{r_b-r_t}\right)\sin(n\theta), \quad (24)$$

with $W^*=\eta h$, where $\eta$ represents the size of the initial imperfection ($\eta<1$).

The Ritz method of energy is used, basing the minimization energy principle, i.e

$$\frac{\partial U_T}{\partial U}=0, \quad (25)$$
$$\frac{\partial U_T}{\partial V}=0, \quad (26)$$
$$\frac{\partial U_T}{\partial W}=0, \quad (27)$$

leads to

$$\lambda_{11}U+\lambda_{12}W=0, \quad (28)$$
$$\lambda_{21}V+\lambda_{22}W^2+\lambda_{23}WW^*=0, \quad (29)$$
$$\lambda_{31}W^3+\lambda_{32}W^2W^*+\lambda_{33}WW^{*2}+\lambda_{34}WV+\lambda_{35}W^*V+\lambda_{36}W\Delta T+\lambda_{37}W^*\Delta T+\lambda_{38}U+\lambda_{39}W=0, \quad (30)$$

where $\lambda_{ij}$ is presented as

$$\lambda_{11}=\int_{r_t}^{r_b}\left[\left(\frac{\overline{A}_{66}n^2+\overline{A}_{22}}{r}\right)\pi\sin^2 2\lambda+\frac{4\overline{A}_{12}m\pi^2}{r_b-r_t}\cos 2\lambda\sin 2\lambda+\frac{4\overline{A}_{11}m^2r\pi^3}{\left(r_b-r_t\right)^2}\cos^2 2\lambda\right]dr,$$

$$\lambda_{12}=\int_{r_t}^{r_b}\left\{\left(\frac{\left(\overline{B}_{66}+\overline{B}_{22}\right)n^2}{r^2}+\frac{\overline{B}_{12}m^2\pi^2}{\left(r_1-r_t\right)^2}-\frac{\overline{A}_{12}+\overline{A}_{22}}{R_m}\right)\pi\sin\lambda\sin2\lambda-\frac{\overline{B}_{66}mn^2+\overline{B}_{22}m}{\left(r_b-r_t\right)r}\pi^2\sin2\lambda\cos\lambda\right.$$
$$\left.+\left(2\frac{\overline{B}_{11}m^3\pi^2r}{\left(r_b-r_t\right)^3}-\frac{2\left(\overline{A}_{12}+\overline{A}_{11}\right)rm}{\left(r_b-r_t\right)R}+\frac{2\overline{B}_{12}mn^2}{\left(r_1-r_t\right)r}\right)\pi^2\sin\lambda\cos2\lambda-\frac{2\overline{B}_{12}m^2\pi^3}{\left(r_b-r_t\right)^2}\cos\lambda\cos2\lambda\right\}dr,$$

$$\lambda_{21}=\int_{r_t}^{r_b}\left[\overline{A}_{66}r^3\left(\frac{m\pi}{\left(r_b-r_t\right)r}\cos\lambda-\frac{1}{r^2}\sin\lambda\right)^2\pi+\frac{4\overline{A}_{22}\pi n^2}{r}\sin^2\lambda\right]dr,$$

$$\lambda_{22}=\int_{r_t}^{r_b}\left\{\frac{1}{2}\frac{\overline{A}_{66}rm\pi^2n}{r_b-r_t}\left[\frac{m\pi}{\left(r_b-r_t\right)r}\cos^2\lambda\cos\lambda-\frac{1}{r^2}\sin^2\lambda\cos\lambda\right]-\frac{1}{2}\frac{\overline{A}_{12}m^2\pi^3n}{\left(r_b-r_t\right)^2}\cos^2\lambda\sin\lambda+\frac{1}{2}\frac{n^3\overline{A}_{22}\pi}{r^2}\sin^3\lambda\right\}dr,$$

$$\lambda_{23}=\int_{r_t}^{r_b}\left\{\frac{\overline{A}_{66}rm\pi^2n}{r_b-r_t}\left[\frac{m\pi}{\left(r_b-r_t\right)r}\cos^2\lambda\sin\lambda-\frac{1}{r^2}\sin^2\lambda\cos\lambda\right]+\frac{\overline{A}_{12}m^2\pi^3n}{\left(r_b-r_t\right)^2}\cos^2\lambda\sin\lambda+\frac{n^3\overline{A}_{22}\pi}{r^2}\sin^3\lambda\right\}dr,$$

$$\lambda_{31}=\int_{r_t}^{r_b}\left[\frac{3\overline{A}_{11}m^4\pi^5r}{8\left(r_b-r_t\right)^4}\cos^4\lambda+\frac{3\overline{A}_{22}n^4\pi}{8r^3}\sin^4\lambda+\frac{\left(2\overline{A}_{66}+\overline{A}_{12}\right)m^2\pi^3n^2}{4\left(r_b-r_t\right)^2r}\cos^2\lambda\sin^2\lambda\right]dr,$$

$$\lambda_{32}=\int_{r_t}^{r_b}\left[\frac{9\overline{A}_{11}m^4\pi^5r}{8\left(r_b-r_t\right)^4}\cos^4\lambda+\frac{9\overline{A}_{22}n^4\pi}{8r^3}\sin^4\lambda+3\frac{\left(2\overline{A}_{66}+\overline{A}_{12}\right)m^2\pi^3n^2}{4\left(r_b-r_t\right)^2r}\sin^2\lambda\cos^2\lambda\right]dr,$$

$$\lambda_{33}=\int_{r_t}^{r_b}\left[\frac{3\overline{A}_{11}m^4\pi^5r}{4\left(r_b-r_t\right)^4}\cos^4\lambda+\frac{3\overline{A}_{22}n^4\pi}{4r^3}\sin^4\lambda+\frac{\left(2\overline{A}_{66}+\overline{A}_{12}\right)m^2\pi^3n^2}{2\left(r_b-r_t\right)^2r}\cos^2\lambda\sin^2\lambda\right]dr,$$

$$\lambda_{34}=\int_{r_t}^{r_b}\left\{\frac{\overline{A}_{66}rm\pi^2n}{r_b-r_t}\left[\frac{m\pi}{\left(r_b-r_t\right)r}\cos^2\lambda\sin\lambda-\frac{1}{r^2}\sin^2\lambda\cos\lambda\right]-\frac{\overline{A}_{12}m^2\pi^3n}{\left(r_b-r_t\right)^2}\cos^2\lambda\sin\lambda+\frac{\overline{A}_{22}n^3\pi}{r^2}\sin^3\lambda\right\}dr,$$

$$\lambda_{35}=\int_{r_t}^{r_b}\left\{\frac{\overline{A}_{66}rm\pi^2n}{r_b-r_t}\left[\frac{m\pi}{\left(r_b-r_t\right)r}\cos^2\lambda\sin\lambda-\frac{1}{r^2}\sin^2\lambda\cos\lambda\right]-\frac{\overline{A}_{12}m^2\pi^3n}{\left(r_b-r_t\right)^2}\cos^2\lambda\sin\lambda+\frac{\overline{A}_{22}n^3\pi}{r^2}\sin^3\lambda\right\}dr,$$

$$\lambda_{36}=\int_{r_t}^{r_b}\left[-\frac{\Phi_{1\theta}n^2\pi}{r}\sin^2\lambda-\frac{\Phi_{1r}rm^2\pi^3}{\left(r_b-r_t\right)^2}\cos^2\lambda\right]dr,$$

$$\lambda_{37}=\int_{r_t}^{r_b}\left[-\frac{\Phi_{1\theta}n^2\pi}{r}\sin^2\lambda-\frac{\Phi_{1r}rm^2\pi^3}{\left(r_b-r_t\right)^2}\cos^2\lambda\right]dr,$$

$$\lambda_{38}=\int_{r_t}^{r_b}\left\{\left[\frac{\left(\overline{B}_{66}+\overline{B}_{22}\right)n^2}{r^2}-\frac{\overline{A}_{12}+\overline{A}_{22}}{R}+\frac{\overline{B}_{12}m^2\pi^2}{\left(r_b-r_t\right)^2}\right]\pi\sin\lambda\sin2\lambda-\frac{\left(\overline{B}_{66}n^2+\overline{B}_{22}\right)m\pi^2}{\left(r_b-r_t\right)r}\cos\lambda\sin2\lambda\right.$$
$$\left.+\left[\frac{2\overline{B}_{11}m^3\pi^4r}{\left(r_b-r_t\right)^3}+\frac{2\overline{B}_{12}mn^2\pi^2}{r\left(r_b-r_t\right)}-\frac{2\left(\overline{A}_{12}+\overline{A}_{11}\right)m\pi^2r}{\left(r_b-r_t\right)R}\right]\sin\lambda\cos2\lambda-\frac{2\overline{B}_{12}m^2\pi^3r}{\left(r_b-r_t\right)^2r}\cos\lambda\cos2\lambda\right\}dr,$$

$$\lambda_{39}=\int_{r_t}^{r_b}\left\{\left[2\frac{\bar{D}_{12}m^2\pi^3n^2}{r\left(r_b-r_t\right)^2}+\frac{\left(\bar{A}_{11}+2\bar{A}_{12}+\bar{A}_{22}\right)r\pi}{R^2}+\frac{\bar{D}_{11}m^4\pi^5r}{\left(r_b-r_t\right)^4}-\frac{2\left(\bar{B}_{12}+\bar{B}_{22}\right)\pi n^2}{Rr}\right.\right.$$
$$\left.-\frac{2\left(\bar{B}_{11}+\bar{B}_{12}\right)m^2\pi^3r}{R\left(r_b-r_t\right)^2}\right]\sin^2\lambda+\left[\frac{2\left(\bar{B}_{12}+\bar{B}_{22}\right)m\pi^2}{R\left(r_b-r_t\right)}-2\frac{\bar{D}_{12}m^3\pi^4}{\left(r_b-r_t\right)^3}\right]\sin\lambda\cos\lambda$$
$$\left.+\bar{D}_{22}\frac{\pi}{r}\left(-\frac{n^2}{r}\sin\lambda+\frac{m\pi}{\left(r_b-r_t\right)}\cos\lambda\right)^2+\frac{n^2\pi}{r}\bar{D}_{66}\left(-\frac{\sin\lambda}{r}+\frac{m\pi}{\left(r_b-r_t\right)}\cos\lambda\right)^2\right\}dr,\ \text{with}\ \lambda=\frac{m\pi\left(r-r_t\right)}{r_b-r_t}.$$

By solving Eqs. (28) and (29), the formulas for $U$ and $V$ are determined. In which $U$ and $V$ are explicitly dependent on $W$ and $\Delta T$. These derived results are then substituted back into Eq. (30), yielding

$$a_1WW^{*2}+a_2W^2W^*+a_3W^3+a_4W+a_5W\Delta T+a_6W^*\Delta T=0, \quad (31)$$

where

$$a_1=\lambda_{35}\eta_{22}+\lambda_{33};\ \ a_2=\lambda_{35}\eta_{21}+\lambda_{34}\eta_{22}+\lambda_{32};$$
$$a_3=\lambda_{34}\eta_{21}+\lambda_{31};\ a_4=\lambda_{38}\eta_{11}+\lambda_{39};\ a_5=\lambda_{36};$$
$$a_6=\lambda_{37};\eta_{11}=-\frac{\lambda_{12}}{\lambda_{11}};\ \ \eta_{21}=-\frac{\lambda_{22}}{\lambda_{21}};\ \ \eta_{22}=-\frac{\lambda_{23}}{\lambda_{21}};$$

Eq. (31) is used to investigate the nonlinear thermal postbuckling curves of stiffened FG-GPLRC SASCs/APLs. From Eq. (31), the expression of $\Delta T$ is obtained as

To examine the nonlinear thermal postbuckling response of stiffened FG-GPLRC SASCs/APLs, Eq. (31) is utilized. From this equation, the corresponding form of $\Delta T$ can be derived as

$$\Delta T=-\frac{a_1WW^{*2}+a_2W^2W^*+a_3W^3+a_4W}{a_5W+a_6W^*} \quad (32)$$

From Eq. (32), the thermal buckling load is determined by setting $W\to 0$ and $\eta=0$ as

$$\Delta T_b=-\frac{a_4}{a_5}, \quad (33)$$

The critical thermal buckling load is obtained from Eq. (33) by applying the condition $\Delta T_{crb}=\min\Delta T_b$ vs. $(m,n)$.

## 5. Numerical results and discussions

In the following illustration section, copper-matrix/GPLs stiffened SASCs and APLs are considered, with GPL material and geometric parameters taken from Ref. [39].

### 5.1. Validations

To evaluate the validity of the proposed analytical method and the current mathematical expressions, the critical thermal buckling loads of unstiffened FG-GPLRC APLs and SASCs were compared with the finite element results as presented in Table 2. The results obtained show good agreement between the current approach and the numerical simulation results.

### 5.2. Numerical examples

Table 3 illustrates the effect of circumferential stiffeners on the critical thermal buckling loads of FG-GPLRC SASCs and APLs for different total GPL mass fractions $\omega_{GPL}$. For both SASCs and APLs, the addition of circumferential stiffeners significantly increases the critical thermal buckling load compared to the unstiffened structures. In addition, the effect of the total mass fraction of GPLs is also significant. The critical thermal buckling load increases when the total mass fraction of GPLs increases. This indicates the effectiveness of the GPL reinforcement phase in enhancing the thermal resistance of FG-GPLRC SASCs and APLs. Table 4 examines the critical thermal load of the SASCs and the APLs with different material distribution patterns. For the illustrative data set, the V-A type FG-GPLRC SASC exhibits the largest critical thermal load among SASCs, while the critical thermal buckling load of A-V type FG-GPLRC SASC is the smallest. For APLs, the largest critical thermal buckling load is recorded corresponding to the X-X type FG-GPLRC, and the smallest is corresponding to O-O

type FG-GPLRC. This is significant for the designers when selecting the appropriate material model for FG-GPLRC stiffened SASCs and APLs. Furthermore, the influence of the $r_b / R$ ratio is also investigated in Table 4. Clearly, the critical thermal buckling load of the stiffened SASCs decreases as the $r_b / R$ ratio decreases. In other words, the critical thermal buckling load of the stiffened SASCs decreases as their shallowness increases.

Figs. 4a-d illustrate the effects of stiffeners on the nonlinear thermal postbuckling responses of SASCs and APLs. It is clear that the stiffeners significantly increase the post-buckling resistance compared to the unreinforced case. This is also noted in Table 2. These results confirm the role of stiffeners in improving the stability of both APLs and SASCs. Unlike the stiffened SSCs and CPLs, the bifurcation phenomenon can be observed in all the cases studied for both perfect APLs and SASCs. At the same time, the snap-through phenomenon is not observed in any of the studied examples. On the other hand, it can be observed that in the case of imperfect SASCs/ APLs, the bifurcation phenomenon does not occur. This phenomenon is also observed in Figs. 5a, b, and d.

**Table 2.** Comparisons of critical thermal buckling loads $\Delta T_{crb}$ (K) of unstiffened FG-GPLRC SASCs and APLs ($r_b = 0.5$ m, $r_t / r_b = 0.5$, $r_b / h = 80$, UD-UD)

| | $\omega_{GPL}$ = 0.1% | $\omega_{GPL}$ = 0.5% | $\omega_{GPL}$ = 1% | $\omega_{GPL}$ = 1.5% |
|---|---|---|---|---|
| Unstiffened APLs | | | | |
| Present | 23.72(1,1)* | 24.36(1,1) | 25.15(1,1) | 25.93(1,1) |
| Simulation (Abaqus) | 24.59(1,1) | 25.29(1,1) | 26.03(1,1) | 26.98(1,1) |
| Difference (%) | 3.67 | 3.82 | 3.50 | 4.05 |
| Unstiffened SASCs | | | | |
| Present | 31.24(**)(1,1) | 32.08 (1,1) | 33.12 (1,1) | 34.14 (1,1) |
| Simulation (Abaqus) | 32.42 (1,1) | 33.33 (1,1) | 34.32 (1,1) | 35.57 (1,1) |
| Difference (%) | 3.78 | 3.90 | 3.62 | 4.19 |

* The buckling modes (m, n),

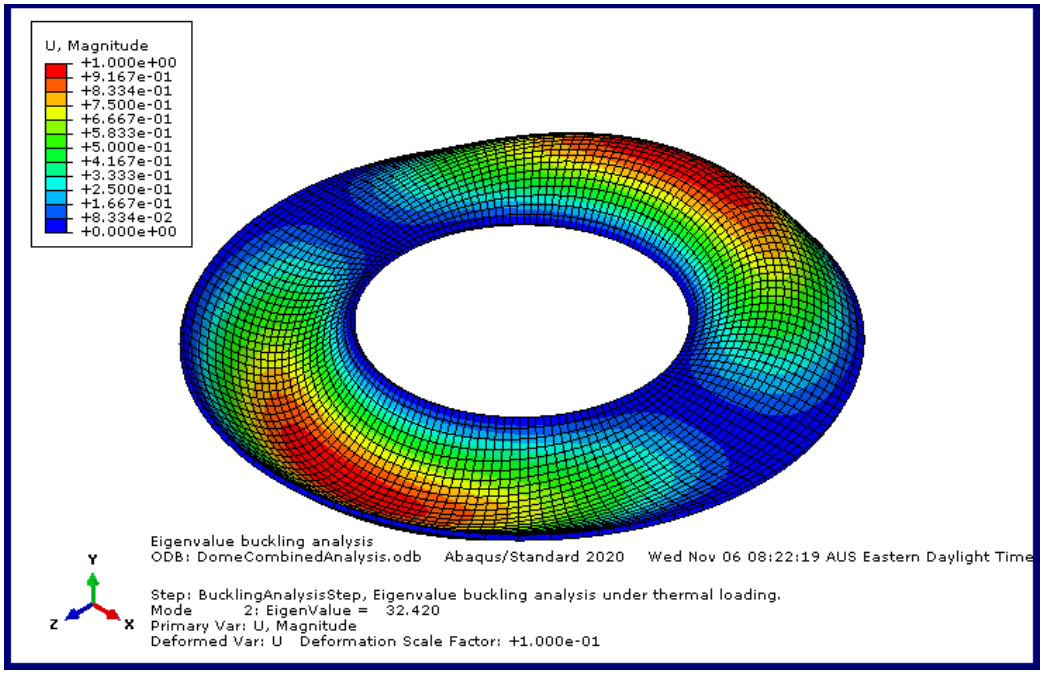


(**)**Fig. 3.** An example of thermal buckling analysis of unstiffened FG-GPLRC SASCs by Abaqus $(m,n) = (1,1)$

**Table 3.** Influence of the stiffeners on critical thermal buckling loads $\Delta T_{crb}$ (K) of APLs and SASCs ($h$ =0.008m, , $r_b/h = 80$, $r_b/R = 0.1$, $r_t/r_b = 0.4$, $n = 4$, $h_{st}/h = 2$, $b_{st}/h = 1$, $\omega_{GPL}$ =1%, UD-UD)

| $\omega_{GPL}$ | SASCs | | APLs | |
|---|---|---|---|---|
| | Unstiffened | Circumferential Stiffener | Unstiffened | Circumferential Stiffener |
| $\omega_{GPL}$ = 0.1% | 43.15 (1,3) | 49.18 (1,2) | 16.91(1,1) | 21.85 (1,1) |
| $\omega_{GPL}$ = 0.5% | 44.20 (1,3) | 50.40 (1,2) | 17.36 (1,1) | 22.45 (1,1) |
| $\omega_{GPL}$ = 1% | 45.50 (1,3) | 51.91 (1,2) | 17.92 (1,1) | 23.20 (1,1) |
| $\omega_{GPL}$ = 1.5% | 46.78 (1,3) | 53.40 (1,2) | 18.47 (1,1) | 23.94 (1,1) |
| $\omega_{GPL}$ = 2% | 48.04 (1,3) | 54.87 (1,2) | 19.01 (1,1) | 24.67 (1,1) |

**Table 4.** Influence of material distribution model on critical thermal load $\Delta T_{crb}$ (K) SASCs and APLs ($h$ =0.009m, $r_b/h = 65$, $r_t/r_b = 0.4$, $h_{st}/h = 2$, $n = 6$, $b_{st}/h = 1$, $\omega_{GPL}$ =0.1%)

| $r_1/R_m$ | UD-UD | X-X | O-O | V-A | A-V |
|---|---|---|---|---|---|
| 0.25 | 170.99 (2,3) | 173.64 (2,3) | 168.39 (2,3) | 175.19(2,3) | 166.81 (2,3) |
| 0.20 | 134.67(1,3) | 135.60 (1,3) | 133.76 (1,3) | 137.76 (1,3) | 131.60 (1,3) |
| 0.18 | 121.06 (1,3) | 121.99 (1,3) | 120.15 (1,3) | 123.94 (1,3) | 118.18 (1,3) |
| 0.15 | 97.21(1,2) | 97.94 (1,2) | 96.50 (1,2) | 99.28(1,2) | 95.15 (1,2) |
| 0.12 | 75.57 (1,2) | 76.29 (1,2) | 74.85 (1,2) | 77.30 (1,2) | 73.83(1,2) |
| 0.10 | 64.25 (1,2) | 64.98 (1,2) | 63.54 (1,2) | 65.77 (1,2) | 62.73(1,2) |
| 0.05 | 46.87 (1,2) | 47.59 (1,2) | 46.15 (1,2) | 47.84 (1,2) | 45.90 (1,2) |
| APLs | 39.32 (1,1) | 40.03 (1,1) | 38.62 (1,1) | 39.63 (1,1) | 40.00 (1,1) |

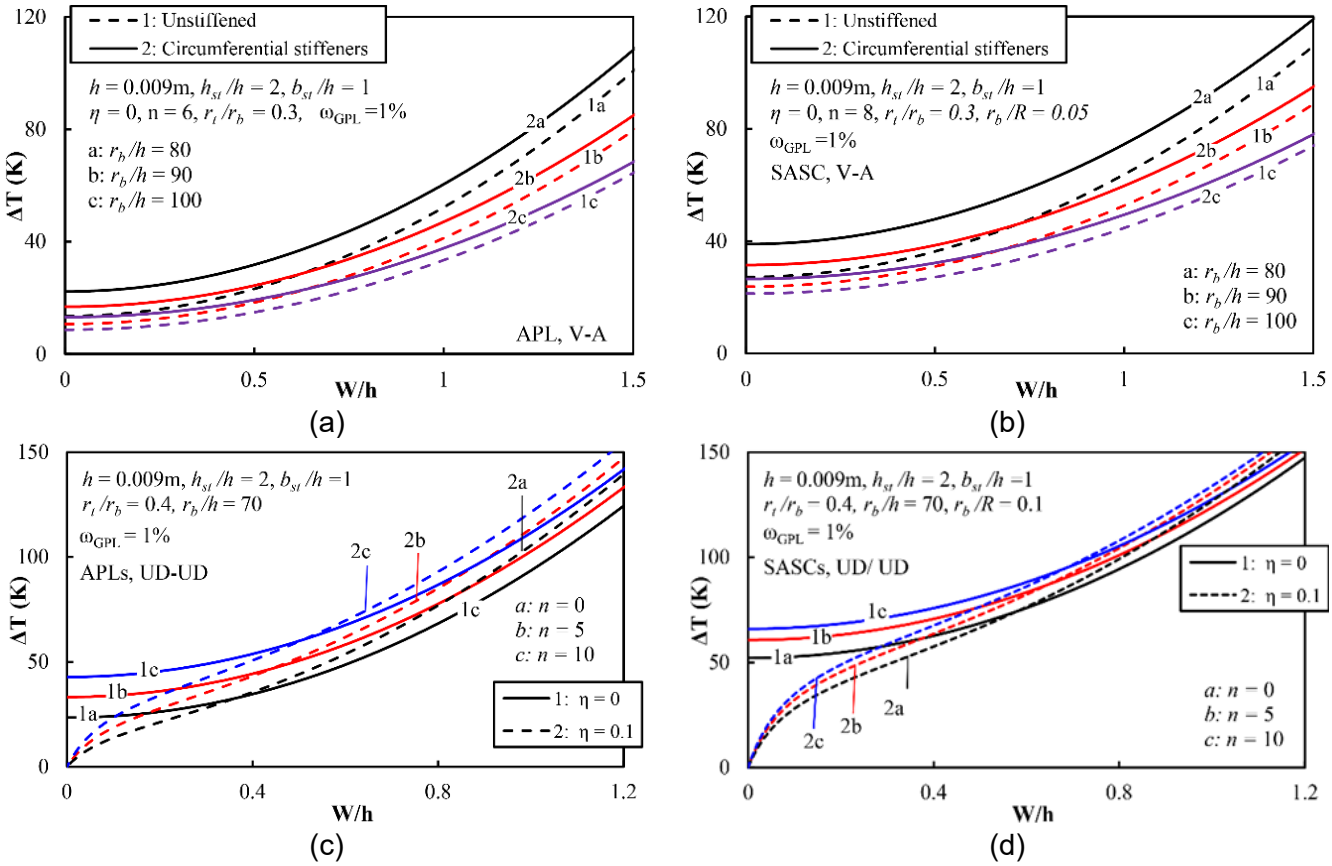


**Fig. 4.** Influences of circumferential stiffeners on nonlinear postbuckling curves of SASCs and APLs

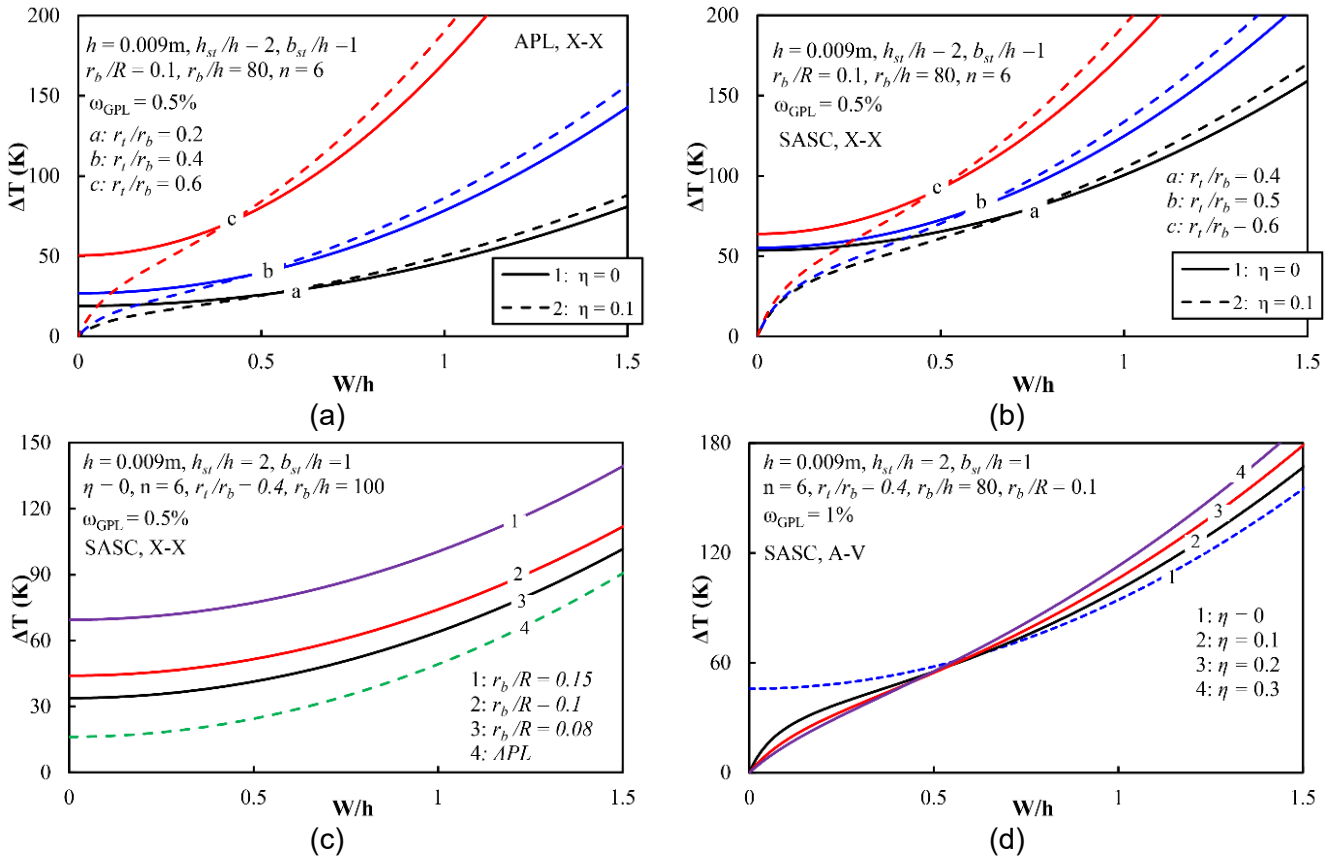


**Fig. 5**. Influences of geometric parameters on nonlinear postbuckling curves of SASCs and APLs

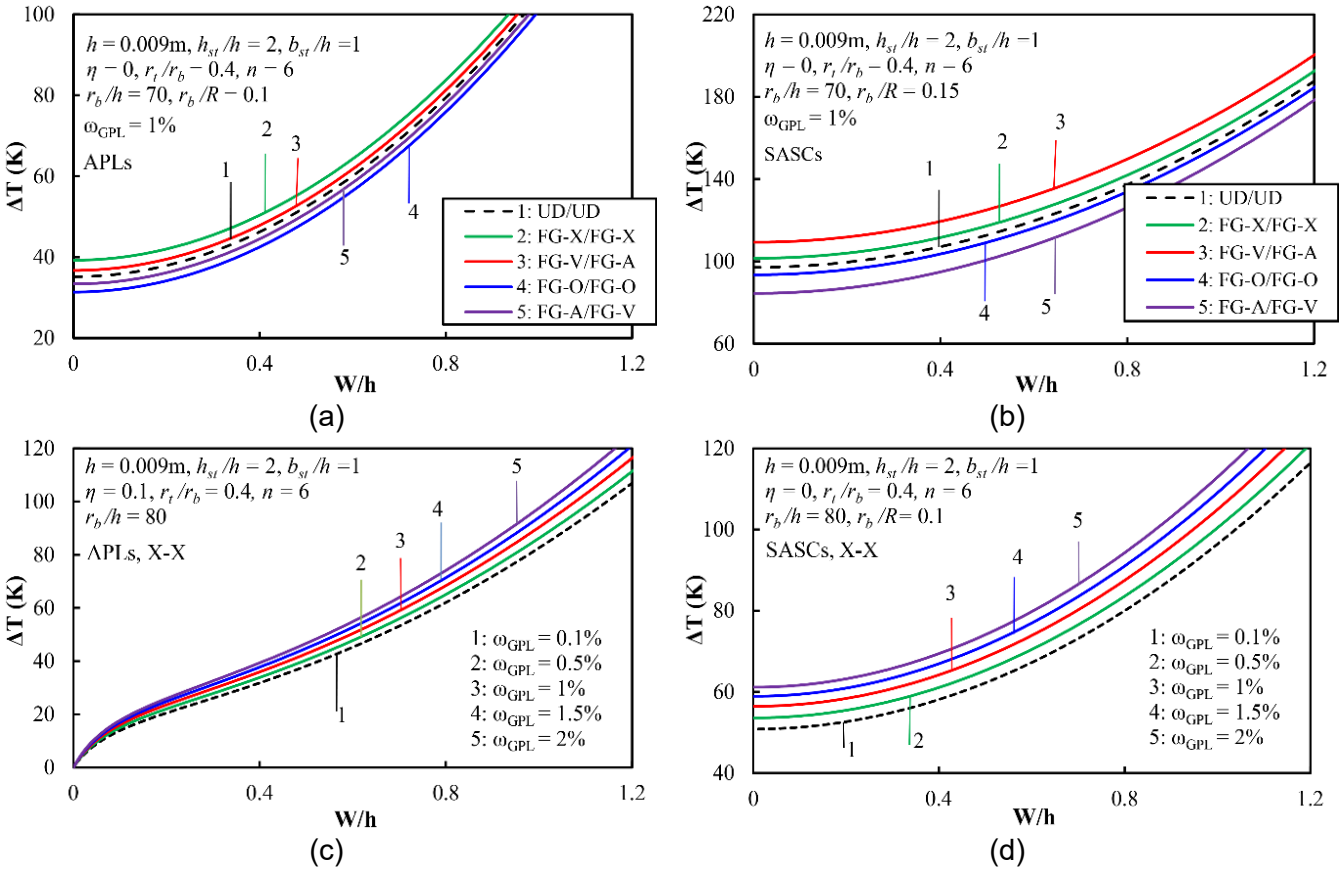


**Fig. 6.** Influences of material distribution model and the total mass fraction of GPLs $\omega_{GPL}$ on nonlinear postbuckling curves of SASCs and APLs

Fig. 5 investigates the significant role of geometric parameters on the nonlinear postbuckling behavior. Specifically, Figs. 5a and b show the influence of the $r_t / r_b$ ratios on the postbuckling curves of SASCs and APLs. Clearly, as the $r_t / r_b$ ratio increases, the postbuckling capacity of both SASC and APL increases. This effect is more pronounced in the region of large deformation. Fig. 5c shows a strong influence of the a/b ratio on the post-buckling curves of SASCs. It is clear that as the ratio a/b decreases, i.e., the shallowness of the SASCs increases, the postbuckling curves become lower. A similar trend is observed in Table 4 for the critical thermal buckling load.

The effect of the imperfections in the SASC is shown in Fig. 5d. It can be observed that, in the small deflection region, the postbuckling curves decrease as the imperfections increase. Conversely, in the large deflection region, the opposite trend is observed. The postbuckling curves appear to intersect at a certain strain, where the trend reversal occurs.

Fig. 6 investigates the nonlinear postbuckling curves of stiffened FG-GPLRC SASCs and APLs with different material models and total mass fraction of GPLs. The obtained trends in Figs. 6a-d are in full agreement with the results shown in Tables 3 and 4. Specifically, in Figs. 6a and b, the V-A SASC has the highest postbuckling curve among the SASCs, while the postbuckling curve of the A-V SASC is the lowest. For APL, the highest postbuckling curve corresponds to the X-X type, and the lowest one corresponds to O-O type. Figs. 6c and 6d once again show that increasing the total mass fraction of GPLs positively affects the thermal load-carrying capacity of stiffened SASCs and APLs.

## 6. Conclusion

By combining the extended smeared stiffener technique, Donnell's classical shell theory, and von Kármán geometric nonlinearity, the nonlinear thermal buckling and postbuckling behaviors of FG-GPLRC SASCs and APLs stiffened by a circumferential stiffener system were presented. Some notable findings can be drawn as follows:

- Circumferential stiffeners help improve the thermal load capacity of SACs and APLs. The bifurcation buckling phenomenon can be observed in all the cases studied for both perfect APLs and SASCs.

- For the illustrative data set, the V-A SASC exhibits the largest load-bearing capacity among SASCs, while the A-V SASC shows the smallest load-bearing capacity. Meanwhile, for APLs, the largest load-bearing capacity is recorded corresponding to the X-X type, and the smallest corresponding to O-O type.

- Geometric and material parameters have a significant impact on the thermal stability responses.

**Acknowledgments**

This research is funded by Vietnam National Foundation for Science and Technology Development (NAFOSTED) under grant number 107.02-2023.45

**References**

[1] A. Kalnins, P.M. Naghdi. (1960). Axisymmetric Vibrations of Shallow Elastic Spherical Shells. *The Journal of the Acoustical Society of America*, 32(3), 342–347. https://doi.org/10.1121/1.1908055

[2] P.L. Grossman, B. Koplik, Y.-Y. Yu. (1969). Nonlinear Vibrations of Shallow Spherical Shells. *Journal of Applied Mechanics*, 36(3), 451–458. https://doi.org/10.1115/1.3564701

[3] M. Sathyamoorthy. (1994). Vibrations of Moderately Thick Shallow Spherical Shells at Large Amplitudes. *Journal of Sound and Vibration*, 172(1), 63–70. https://doi.org/10.1006/jsvi.1994.1158

[4] G.P. Dube, S. Joshi, P.C. Dumir. (2001). Nonlinear analysis of thick shallow spherical and conical orthotropic caps using Galerkin's method. *Applied Mathematical Modelling*, 25(9), 755–773. https://doi.org/10.1016/S0307-904X(01)00012-9

[5] Y. Wang, W. Tang, J. Zhang, S. Zhang, Y. Chen. (2019). Buckling of imperfect spherical caps with fixed boundary under uniform external pressure. *Marine Structures*, 65, 1–11. https://doi.org/10.1016/j.marstruc.2019.01.004

[6] Y. Du, F. Pang, L. Sun, H. Li. (2020). A unified formulation for dynamic behavior analysis of spherical cap with uniform and stepped thickness distribution under different edge constraints. *Thin-Walled Structures*, 146, 106445. https://doi.org/10.1016/j.tws.2019.106445

[7] A. Li, X. Ji, S. Zhou, L. Wang, J. Chen, P. Liu. (2021). Nonlinear axisymmetric bending analysis of strain gradient thin circular plate. *Applied Mathematical Modelling*, 89, 363–380. https://doi.org/10.1016/j.apm.2020.08.004

[8] M.S. Ismail, J. Mahmud, A. Jailani. (2023). Buckling of an imperfect spherical shell subjected to external pressure. *Ocean Engineering*, 275, 114118. https://doi.org/10.1016/j.oceaneng.2023.114118

[9] M. Jabbari, A. Mojahedin, E.F. Joubaneh. (2015). Thermal Buckling Analysis of Circular Plates Made of Piezoelectric and Saturated Porous Functionally Graded Material Layers. *Journal of Engineering Mechanics*, 141(4), 04014148.https://doi.org/10.1061/(ASCE)EM.1943-7889.0000872

[10] Y. Kiani. (2017). Axisymmetric static and dynamics snap-through phenomena in a thermally postbuckled temperature-dependent FGM circular plate. *International Journal of Non-Linear Mechanics*, 89, 1–13. https://doi.org/10.1016/j.ijnonlinmec.2016.11.003

[11] R. Saini, S. Saini, R. Lal, I.V. Singh. (2019). Buckling and vibrations of FGM circular plates in thermal environment. *Procedia Structural Integrity*, 14, 362–374. https://doi.org/10.1016/j.prostr.2019.05.045

[12] H. Zhou, K. Han, L. Elmaimouni, X. Wang, J. Yu. (2024). Double Legendre polynomial quadrature-free method for axisymmetric vibration of functionally graded piezoelectric circular plates. *Journal of Vibration and Control*, 30, 598–615. https://doi.org/10.1177/10775463221149087

[13] H. Ahmadi, K. Foroutan. (2021). Nonlinear buckling analysis of FGP shallow spherical shells under thermomechanical condition. *Steel and Composite Structures*, 40(4), 555–570. https://doi.org/10.12989/scs.2021.40.4.555

[14] Y. Fu, S. Hu, Y. Mao. (2014). Nonlinear transient response of functionally graded shallow spherical shells subjected to mechanical load and unsteady temperature field. *Acta Mechanica Solida Sinica*, 27(5), 496–508. https://doi.org/10.1016/S0894-9166(14)60058-6

[15] D.H. Bich, H.V. Tung. (2011). Non-linear axisymmetric response of functionally graded shallow spherical shells under uniform external pressure including temperature effects. *International Journal of Non-Linear Mechanics*, 46(9), 1195–1204. https://doi.org/10.1016/j.ijnonlinmec.2011.05.015

[16] V.T.T. Anh, N.D. Duc. (2016). Nonlinear response of a shear deformable S-FGM shallow spherical shell with ceramic-metal-ceramic layers resting on an elastic foundation in a thermal environment. *Mechanics of Advanced Materials and Structures*, 23(8), 926–934. https://doi.org/10.1080/15376494.2015.1059527

[17] N.T. Phuong, V.H. Nam, D.T. Dong. (2020). Nonlinear vibration of functionally graded sandwich shallow spherical caps resting on elastic foundations by using first-order shear deformation theory in thermal environment. *Journal of Sandwich Structures & Materials*, 22(4), 1157–1183. https://doi.org/10.1177/1099636218782645

[18] L.N. Ly, D.T.N. Thu, D.T. Dong, V.M. Duc, B.T. Tu, N.T. Phuong, V.H. Nam. (2023). A Novel

Analytical Approach for Nonlinear Thermo-Mechanical Buckling of Higher-Order Shear Deformable Porous Circular Plates and Spherical Caps with FGM Face Sheets. *International Journal of Applied Mechanics*, 15(05), 2350035. https://doi.org/10.1142/S1758825123500357

[19] A.R. Barzegar, M. Fadaee. (2018). Thermal vibration analysis of functionally graded shallow spherical caps by introducing a decoupling analytical approach. *Applied Mathematical Modelling*, 58, 473–486. https://doi.org/10.1016/j.apm.2018.02.018

[20] M. Javani, Y. Kiani, M.R. Eslami. (2021). Geometrically nonlinear free vibration of FG-GPLRC circular plate on the nonlinear elastic foundation. *Composite Structures*, 261, 113515. https://doi.org/10.1016/j.compstruct.2020.113515

[21] C. Chu, M.S.H. Al-Furjan, R. Kolahchi, A. Farrokhian. (2023). A nonlinear Chebyshev-based collocation technique to frequency analysis of thermally pre/post-buckled third-order circular sandwich plates. *Communications in Nonlinear Science and Numerical Simulation*, 118, 107056. https://doi.org/10.1016/j.cnsns.2022.107056

[22] C.H. Thai, P.P.-Van. (2020). A meshfree approach using naturally stabilized nodal integration for multilayer FG GPLRC complicated plate structures. *Engineering Analysis with Boundary Elements*, 117, 346–358.https://doi.org/10.1016/j.enganabound.2020.04.001

[23] Z. Dai, H. Tang, S. Wu, M. Habibi, Z. Moradi, H.E. Ali. (2023). Nonlinear consecutive dynamic instabilities of thermally shocked composite circular plates on the softening elastic foundation. *Thin-Walled Structures*, 186, 110645. https://doi.org/10.1016/j.tws.2023.110645

[24] Y. Heydarpour, P. Malekzadeh, F. Gholipour. (2019). Thermoelastic analysis of FG-GPLRC spherical shells under thermo-mechanical loadings based on Lord-Shulman theory. *Composites Part B: Engineering*, 164, 400–424.https://doi.org/10.1016/j.compositesb.2018.12.073

[25] D. Liu, Y. Zhou, J. Zhu. (2021). On the free vibration and bending analysis of functionally graded nanocomposite spherical shells reinforced with graphene nanoplatelets: Three-dimensional elasticity solutions. *Engineering Structures*, 226, 111376. https://doi.org/10.1016/j.engstruct.2020.111376

[26] T.P. Nguyen, T.D. Dang, T.T. Bui, M.D. Vu, K. Le-Nguyen, T.H. Pham, H.N. Vu. (2024). Nonlinear thermo-mechanical axisymmetric stability of FG-GPLRC spherical shells and circular plates resting on nonlinear elastic medium. *Ships and Offshore Structures*, 19(6), 820–830. https://doi.org/10.1080/17445302.2023.2214489

[27] T.T. Bui, M.D. Vu, N.N. Pham, V.D. Cao, H.N. Vu. (2024). Nonlinear thermo-mechanical dynamic buckling and vibration of FG-GPLRC circular plates and shallow spherical shells resting on the nonlinear viscoelastic foundation. *Archive of Applied Mechanics*, 94, 3715–3729. https://doi.org/10.1007/s00419-024-02691-6

[28] N.L. Le, T.T. Bui, T.N.T. Duong, T.D. Dang, M.D. Vu, T.P. Nguyen. (2023). Nonlinear thermo-mechanical buckling and postbuckling of sandwich FG-GPLRC spherical caps and circular plates with porous core by using higher-order shear deformation theory. *Journal of Thermoplastic Composite Materials*, 36(10), 4083–4105. https://doi.org/10.1177/08927057221147827

[29] V.H. Nam, T.Q. Minh, P.T. Hieu, V.T. Hung, B.T. Tu, N.T.T. Hoai, D.T. Dong. (2023). A new analytical approach for nonlinear thermo-mechanical postbuckling of FG-GPLRC circular plates and shallow spherical caps stiffened by spiderweb stiffeners. *Thin-Walled Structures*,

193, 111296. https://doi.org/10.1016/j.tws.2023.111296

[30] H.N. Vu, Q.M. Tran, V.T. Nguyen, T.H. Pham, T.P. Nguyen. (2025). Nonlinear static and dynamic buckling analysis of GPL-reinforced spherical caps and circular plates with porous core and stepped spiderweb stiffeners. *Applied Mathematical Modelling*, 145, 116123. https://doi.org/10.1016/j.apm.2025.116123

[31] H.N. Vu, V.T. Nguyen, N.N. Pham, Q.M. Tran, M.D. Vu. (2025). Nonlinear vibration responses of GPL-reinforced circular plates and spherical shells stiffened by multi-step spiderweb stiffeners with piezoelectric layer. *Ships and Offshore Structures*, 1–19. https://doi.org/10.1080/17445302.2025.2537944

[32] P.C. Dumir, G.P. Dube, A. Mallick. (2005). Axisymmetric buckling of laminated thick annular spherical cap. *Communications in Nonlinear Science and Numerical Simulation*, 10(2), 191–204. https://doi.org/10.1016/S1007-5704(03)00124-2

[33] Z. Pu, Q. Xu, Y. Yang, Q. Luo, Y. Li. (2024). Symmetric and asymmetric vibration and buckling of a thermal rotating annular-plate with Pasternak foundation. *Thin-Walled Structures*, 204, 112342. https://doi.org/10.1016/j.tws.2024.112342

[34] H. Li, F. Pang, H. Chen. (2019). A semi-analytical approach to analyze vibration characteristics of uniform and stepped annular-spherical shells with general boundary conditions. *European Journal of Mechanics - A/Solids*, 74, 48–65. https://doi.org/10.1016/j.euromechsol.2018.10.017

[35] V.H. Nam, N.T. Phuong, D.H. Bich. (2020). Buckling analysis of parallel eccentrically stiffened functionally graded annular spherical segments subjected to mechanic loads. *Mechanics of Advanced Materials and Structures*, 27(7), 569–578. https://doi.org/10.1080/15376494.2018.1487608

[36] S.S. Mirjavadi, M. Forsat, M.R. Barati, A.M.S. Hamouda. (2022). Geometrically nonlinear vibration analysis of eccentrically stiffened porous functionally graded annular spherical shell segments. *Mechanics Based Design of Structures and Machines*, 50(6), 2206–2220. https://doi.org/10.1080/15397734.2020.1771729

[37] H. Hu, R. Zhong, Q. Wang. (2025). Effect of distributed DVAs on stochastic dynamic behaviors of FG-GPLRC annular plates. *Advances in Engineering Software*, 209, 103982.https://doi.org/10.1016/j.advengsoft.2025.103982

[38] M. Safarpour, A. Ghabussi, F. Ebrahimi, M. Habibi, H. Safarpour. (2020). Frequency characteristics of FG-GPLRC viscoelastic thick annular plate with the aid of GDQM. *Thin-Walled Structures*, 150, 106683. https://doi.org/10.1016/j.tws.2020.106683

[39] Y. Wang, R. Zeng, M. Safarpour. (2022). Vibration analysis of FG-GPLRC annular plate in a thermal environment. *Mechanics Based Design of Structures and Machines*, 50(1), 352–370. https://doi.org/10.1080/15397734.2020.1719508

[40] M. Safarpour, A. Rahimi, A. Alibeigloo, H. Bisheh, A. Forooghi. (2021). Parametric study of three-dimensional bending and frequency of FG-GPLRC porous circular and annular plates on different boundary conditions. *Mechanics Based Design of Structures and Machines*, 49(5), 707–737. https://doi.org/10.1080/15397734.2019.1701491